

## Simulation of binary collision of liquid drops using smoothed particle hydrodynamics with adaptive spatial resolution

Xinshuo Zhang <sup>1,2</sup> and Xiufeng Yang <sup>1,\*</sup>

<sup>1</sup>*School of Aerospace Engineering, Beijing Institute of Technology, Beijing 100081, China*

<sup>2</sup>*Department of Mechanical, Maritime and Materials Engineering, Delft University of Technology, Delft 2628CD, Netherlands*



(Received 11 January 2023; revised 16 May 2023; accepted 12 July 2023; published 7 August 2023)

The binary collision of water drops in the air is studied by two-dimensional numerical simulation utilizing smoothed particle hydrodynamics with adaptive spatial resolution. The numerical method is validated by comparing the simulation with experiment. Three basic modes of equal-size drop collision are observed in numerical simulations at Weber number  $3 \leq We \leq 120$  and impact parameter  $0 \leq x \leq 0.8$ , namely, reflexive separation, stretching separation, and coalescence collision. Based on the numerical results of different collision modes, the specific phenomena, evolution patterns, and physical principles are discussed. In particular, the detailed processes of the necking phenomenon and the propagation of surface wave in separation collision are obtained, corroborating the “end-pinching” theory proposed in the literature. At higher Weber numbers, the recoalescence of satellite drops is observed. The collision of unequal-size drops is also investigated. The effects of three dimensionless parameters, namely, drop diameter ratio, Weber number, and impact parameter are discussed. The physical mechanisms of some special phenomena are expressed in detail.

DOI: [10.1103/PhysRevE.108.025302](https://doi.org/10.1103/PhysRevE.108.025302)

### I. INTRODUCTION

Drop collision is a widespread physical phenomenon in nature and engineering applications such as thermal spray, spray cooling, and the internal combustion engine [1]. The collision process is often accompanied by the deformation, aggregation, and separation of the drops, which has a significant impact on the shape, size, and velocity of the drops [2], forming a drop system with complex microscopic composition and macroscopic characteristics. For example, in an internal combustion engine, a large number of drops are generated after the atomization of liquid fuel injected in the cylinder. Especially in the core area of the fuel spray with high drop density, the collision phenomenon plays a decisive role in the geometric features and the state of motion of the drops [3], which can directly change the characteristics of the spray field in the cylinder. Thus drop collision has a significant impact on the efficiency of the internal combustion engine [4]. In addition, the collision phenomenon of drops is also encountered in ink-jet printing, additive manufacturing, and liquid rocket engines [5–7]. Therefore, the study of drop collision is of great importance for engineering applications.

Among the complex drop collision phenomena, the opposite collision of two spherical drops is a basic case, as illustrated in Fig. 1. As the drops approach each other, the gas in the gap is compressed, due to which the drops are deformed with the opposite motion hindered. Most of the kinetic energy of the opposite motion is converted into capillary potential energy, while a small part of it is dissipated through the

liquid flow inside the drops and the gas flow in the gap. If the scale of the gap finally reaches the range of intermolecular interaction, the drops will merge; otherwise they will rebound.

The drop collision phenomenon is controlled by a number of factors, the results of which depend not only on the motion parameters of the drops but also on the physical properties of the liquid and the surrounding gas, such as surface tension coefficient, viscosity, etc. In the present paper, the binary collision of drops occurs at room temperature and atmospheric pressure. The drop collision problem in this situation can be described by liquid density  $\rho$ ; viscosity  $\mu$ ; surface tension coefficient  $\sigma$ ; the diameters of two drops, respectively,  $d_l$  and  $d_s$ ; and their velocities, respectively,  $u_l$  and  $u_s$ . Here the subscript “*s*” stands for the smaller drop, and “*l*” for the larger one.

For a more concise description of motion, the relative velocity is often used for the collision system of only two drops:

$$u = u_l + u_s. \quad (1)$$

In addition, the relative position of the drops will also have a significant impact on the result of collision. Therefore, the impact parameter  $X$  is defined to represent the distance from the center of one drop to the relative velocity vector of another drop.

According to dimensional analysis on the variables mentioned above, four dimensionless parameters can be obtained: Reynolds number  $Re$ , Weber number  $We$ , drop diameter ratio  $\Delta$ , and dimensionless impact parameter  $x$ , which are defined

\*xyang@bit.edu.cn

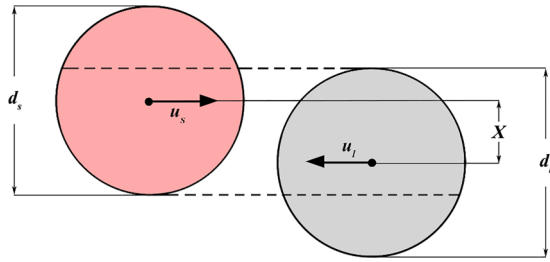


FIG. 1. Schematic diagram of drop collision.

as follows:

$$\text{Re} = \frac{\rho d_l u}{\mu}, \quad (2)$$

$$\text{We} = \frac{\rho d_s u^2}{\sigma}, \quad (3)$$

$$\Delta = \frac{d_s}{d_l}, \quad (4)$$

$$x = \frac{2X}{d_l + d_s}. \quad (5)$$

The Reynolds number  $\text{Re}$  characterizes the effect of inertia and viscous forces. Previous studies showed that within the range of Reynolds number 500–4000, the outcome of binary drop collision does not vary significantly with the Reynolds number [8]. Therefore, the collision phenomenon can be described by the Weber number  $\text{We}$ , drop diameter ratio  $\Delta$ , and dimensionless impact parameter  $x$ . According to the definition,  $x = 0$  and  $x = 1$  represent head-on and grazing collisions, respectively. In the case of  $0 < x < 1$ , the system experiences off-center collision.

In the literature, a number of experiments have been carried out to study the problem of drop collision. Brazier-Smith *et al.* [8] conducted an experimental study on the collision of water drops, and established their prediction equation for collision outcomes based on energy theory. Ashgriz and Poo [9] carried out more systematic experiments on the collision of water drops. With the aid of high-speed video technology, the drop morphology and mass transferring in the collision process was recorded in detail. By summarizing the outcomes under different collision parameters, the range of various collision regions was measured. Relevant theoretical models were proposed to predict reflexive and stretching separations. In addition, the collision of nonwater drops has also been experimentally investigated, from which more complex collision phenomena were discovered. Jiang *et al.* [10] reported on the nonmonotonic behavior of hydrocarbon drop collision, for which phenomenological explanations were provided. Qian and Law [11] conducted experimental research on the binary collision of water and hydrocarbon drops in various gaseous environments at different pressures, extending and unifying previous observations obtained at the atmospheric pressure. Planchette *et al.* [12] investigated the binary collisions of immiscible liquid drops and discussed effective methods for achieving liquid encapsulation. Special mechanisms such as single-reflex separation and crossing separation were experimentally validated and summarized, with the pro-

cess being controlled by the viscosity ratio and momentum ratio.

According to previous studies, the outcomes of drop collision can be generally divided into four categories: bouncing, coalescence, separation, and shattering collisions. For bouncing collision, the contact of two drops is prevented by the compressed gas layer. As a result, the drops deform and rebound without mass transfer. Coalescence refers to the phenomenon where two drops merge permanently after collision. For separation collision, the drops also coalesce briefly after contact; then they break up into multiple subdrops arranged regularly. Shattering collision often occurs at higher velocity, and the drops experience a significant deformation and decompose into a large number of smaller drops. It should be noted that for the collision of drops under atmospheric pressure, which is the main concern of this paper, it is very difficult for bouncing collision to take place [11]. Shattering collision, which has been proved to be dominated by a different mechanism [9], is also not the focus of the present study.

Many experimental investigations in the literature were focused on the outcomes of drop collision and the influencing factors. However, performing analysis and prediction only from the perspective of phenomenology is not satisfactory. Limited by technology, most of the previous experimental work focuses on the observation and summary of phenomena, and much of the underlying physics remains to be explored. In addition, since the actual influencing factors of drop collision are quite complex, it is rather expensive and difficult to conduct detailed experimental investigations on such problems. In contrast, the numerical simulation based on computational fluid dynamics (CFD) has lower cost and better adaptability, and it is hardly affected by external factors. Thus, it is able to overcome many limitations of experimental conditions. By solving the partial differential equations of mass, momentum, and energy, we can obtain information that is difficult to directly measure or observe in experiments. This helps us to understand the drop collision problem at a deep level and also provides convincing evidence for the existing theoretical models.

The simulation of drop collision has to consider the complex interfaces between drops and ambient gas. For mesh based CFD methods, the interface tracking techniques are often required to simulate multiphase flows. The volume of fluid (VOF) model is a commonly used interface tracking technique, and it has the advantage of global and local volume conservation [13]. To simulate drop collision, an improved VOF technique [14] that tracks the gas-liquid interface with the aid of an adaptive mesh refinement algorithm was applied. A consistent geometric VOF method was proposed to simulate vaporizing drops [15]. The level-set method is also an interface tracking technique used in numerous works in the literature. The main advantage of the level-set method is that it is able to naturally capture the change of interface [16]. Coupled with direct numerical simulation, the level-set method can be used to simulate the process of drop impact [17]. An alternative approach for interface capturing is the diffuse-interface method based on the phase field concept [18]. Kajzer and Pozorski [19] proposed a diffuse-interface approach based on the modified conservative Allen-Cahn equation for simulation on low-speed, two-phase flows. The off-center collision of liquid

drops serves as a good example of the method, which is in good agreement with experiments under the given resolution. To improve the capturing of complex interfaces, a promising method is to couple different models, such as the coupling of the level-set and VOF methods [20], and the coupling of the level-set and immersed boundary methods [21].

However, due to the complex deformation of drops such as drop coalescence, rotation, fragmentation, and separation, the simulation of drop collision is still a challenge for CFD. This paper presents a mesh-free particle method based on smoothed particle hydrodynamics (SPH) for the simulation of drop collision. The SPH method was originally proposed to solve the problem of planetary motion in open space [22,23] and then gradually expanded to the fields of free surface flow, multiphase flow, fluid-structure interaction, large deformation, and moving boundary [24–28]. As a pure Lagrangian method, the SPH method completely discards grids. Instead, discrete particles are utilized to describe the motion state and boundary position of the material system. Since the particles are not only interpolation points but also material points carrying physical properties, the system can be pictured quite intuitively. The SPH method has developed rapidly in recent years, because it has a couple of advantages. First, SPH can capture the complex interfaces of different phases without using additional interface capturing techniques. In addition, the breakup and merging of interfaces can be simulated directly without using breakup and merging criteria. Second, SPH is able to simulate the large deformation of fluid or solid. Third, the SPH method has the advantage of mass conservation. Fourth, it is easy in SPH to treat complex geometries and moving boundaries. The SPH method also has some drawbacks, such as the challenges related to accuracy and adaptive resolution. More SPH challenges are defined in Ref. [29].

To save computational costs of CFD simulations, the technique of adaptive resolution is usually applied in simulations with high spatial resolution. For mesh based CFD methods, many techniques of adaptive resolution or mesh refinement have been developed, such as the adaptive octree/quadtree mesh for the VOF [15] and level-set [16] methods, and the adaptive mesh refinement (AMR) algorithm for the lattice Boltzmann method (LBM) [30,31]. Watanabe and Aoki [30] proposed a LBM-AMR method for large-scale free-surface flow simulations on multiple graphics processing units (GPUs). Wu *et al.* [31] developed a mesh refinement procedure called the multi-relaxation-time (MRT) LBM to capture the rapid variation of the flow properties in the near-wall region and perform the simulations on a GPU cluster. However, it is difficult to develop an adaptive resolution algorithm for the SPH method because of the movement of SPH particles. When the SPH method is applied to simulate incompressible flows, the initial particles are usually uniformly distributed in space. This inevitably leads to particles in the “region of no interest” taking up computational resources unnecessarily, hereby incurring high computational costs [32]. In order to solve this problem, a SPH model with adaptive spatial resolution (ASR) [32–34] is employed in the present study to carry out numerical simulations on the binary collision of water drops in the air. The main characteristic of this method is that the particle spacing varies according to the distance between the particles and the gas-liquid interface, so as to real-

ize adaptive particle distribution in the computational domain and improve the computational efficiency. By comparing with relevant experimental results, it is verified that the simulation results are of high credibility within the allowable error range.

The preliminary goal of this work is to study the modes of drop collision and the corresponding characteristics and mechanisms by numerical simulation using the SPH-ASR method. The effects of three dimensionless parameters, namely, the Weber number, impact parameter, and drop diameter ratio, on drop collision are investigated. Through the analysis and induction of simulation results, different collision modes and their boundaries are obtained. Subsequently, the typical physical processes of these collision modes are described in detail, while the physical mechanisms behind some phenomena are discussed.

## II. NUMERICAL METHOD

### A. SPH for fluid mechanics

The basic idea of approximation in the SPH method is as follows: (a) Representing continuous functions and their derivatives as the integral form of smoothing kernel functions; (b) discretizing the computational domain with distributed particles. A field variable on a particle can be approximated by a summation of the values corresponding to the neighboring particles in the support domain.

The integral representation of a function  $f$  by approximation is as follows,

$$\langle f(x) \rangle = \int_{\Omega} f(x') W(x - x', h) dx', \quad (6)$$

where  $x$  is the position vector,  $\Omega$  is the integral domain containing  $x$ , and  $W(x - x', h)$  is the smoothing kernel function with  $h$  the smoothing length.

Subsequently, the above formula is discretized using particle summations as follows,

$$\langle f(x_i) \rangle = \sum_j \frac{m_j}{\rho_j} f_j W(r_{ij}, h), \quad (7)$$

where the subscripts  $i$  and  $j$  denote particles;  $m_j$  and  $\rho_j$ , respectively, represent the mass and density of particles;  $r_{ij}$  is the distance between two particles; and  $N$  is the number of particles. The physical meaning of this step is to discretize continuous material into particles with physical properties.

Similarly, the approximation of the derivative of the function  $f$  can be written as

$$\langle \nabla f(x_i) \rangle = \sum_j \frac{m_j}{\rho_j} (f_j - f_i) \nabla_i W(r_{ij}, h). \quad (8)$$

For fluid dynamics, by applying the above approximation to all relevant terms of governing equations, the discretization of the differential equations in the computational domain can be realized. The Navier-Stokes equations, namely, the continuity equation and the momentum equation, are written in their Lagrangian form,

$$\frac{d\rho}{dt} = -\rho \nabla \cdot \mathbf{u}, \quad (9)$$

$$\frac{d\mathbf{u}}{dt} = \mathbf{g} - \frac{\nabla p}{\rho} + \frac{\mu}{\rho} \nabla^2 \mathbf{u} + \frac{1}{\rho} \mathbf{F}^s, \quad (10)$$

where  $\rho$  is density,  $\mathbf{u}$  is velocity,  $p$  is pressure, and  $\mu$  is the dynamic viscosity. The gravitational acceleration  $\mathbf{g}$  will be

omitted below due to the negligence of gravity in this study. The surface tension  $\mathbf{F}^S$  is defined by the continuum surface force (CSF) model [35] as follows,

$$\mathbf{F}^S = -\sigma\kappa\mathbf{n}\delta^S = \sigma(\nabla \cdot \mathbf{n})\nabla c, \quad (11)$$

where  $\sigma$ ,  $\kappa$ ,  $\mathbf{n}$ ,  $\delta^S$ , and  $c$  denote the coefficient of surface tension, the surface curvature, the surface unit normal, the surface delta function, and a color function, respectively.

In the present work, the kernel function suggested by Yang and Liu [36,37] is employed to get rid of the tensile instability problem that may appear in the SPH simulation of fluid flows,

$$W(s, h) = \frac{1}{3\pi h^2} \begin{cases} s^3 - 6s + 6, & 0 \leq s < 1 \\ (2-s)^3, & 1 \leq s < 2, \\ 0, & 2 \leq s \end{cases} \quad (12)$$

where  $s = r/h$ .

It should be noted that in the SPH method with adaptive spatial resolution, the particle spacing is variable. Thus, the smoothing length should also be variable. The symmetrical expression of kernel function suggested by Hernquist and Katz [38] is utilized to satisfy the conservation of momentum:

$$\overline{W}_{ij} = \frac{1}{2}[W(r_{ij}, h_i) + W(r_{ij}, h_j)], \quad (13)$$

$$\overline{\nabla_i W}_{ij} = \frac{1}{2}[\nabla_i W(r_{ij}, h_i) + \nabla_i W(r_{ij}, h_j)]. \quad (14)$$

In summary, based on the particle approximation principle of the SPH method, the Navier-Stokes equations can be written in discrete form as follows,

$$\frac{d\rho_i}{dt} = \sum_j m_j (\mathbf{u}_i - \mathbf{u}_j) \cdot \overline{\nabla_i W}_{ij}, \quad (15)$$

$$\begin{aligned} \frac{d\mathbf{u}_i}{dt} = & - \sum_j m_j \left( \frac{p_i + p_j}{\rho_i \rho_j} + \Pi_{ij} \right) \overline{\nabla_i W}_{ij} + \sum_j \frac{4m_j \mu_i \mu_j (\mathbf{r}_i - \mathbf{r}_j) \cdot \overline{\nabla_i W}_{ij}}{\rho_i \rho_j (\mu_i + \mu_j) (r_{ij}^2 + \eta)} (\mathbf{u}_i - \mathbf{u}_j) \\ & + \frac{2\sigma_i}{V_i} \sum_j \frac{(\mathbf{n}_i - \mathbf{n}_j) \cdot V_j \overline{\nabla_i W}_{ij}}{|\mathbf{r}_i - \mathbf{r}_j| \cdot V_j \overline{\nabla_i W}_{ij}} \sum_j \frac{V_i^2 + V_j^2}{\rho_i + \rho_j} \overline{\nabla_i W}_{ij}, \end{aligned} \quad (16)$$

where  $\Pi_{ij}$  is the artificial viscosity proposed by Monaghan [39]:

$$\Pi_{ij} = \begin{cases} \frac{-\alpha(c_i + c_j)\mu_{ij} + 2\beta\mu_{ij}^2}{\rho_i + \rho_j}, & (\mathbf{u}_i - \mathbf{u}_j) \cdot (\mathbf{r}_i - \mathbf{r}_j) < 0, \\ 0, & (\mathbf{u}_i - \mathbf{u}_j) \cdot (\mathbf{r}_i - \mathbf{r}_j) \geq 0, \end{cases} \quad (17)$$

$$\mu_{ij} = \frac{(h_i + h_j)(\mathbf{u}_i - \mathbf{u}_j) \cdot (\mathbf{r}_i - \mathbf{r}_j)}{2(r_{ij}^2 + \eta)}. \quad (18)$$

Here  $\alpha$  and  $\beta$  are utilized to regulate the strength of artificial viscosity. The artificial viscosity is used to reduce the nonphysical oscillation in SPH simulations. Since the nonphysical oscillation of the gas SPH particles is larger than the liquid SPH particles in the same simulation, the strength of artificial viscosity for the gas phase is larger than for the liquid phase. In our simulations,  $\alpha = 0.01$  and  $\beta = 0$  for the liquid phase;  $\alpha = 0.1$  and  $\beta = 0.2$  for the gas phase.

### B. Adaptive resolution

In the present work, the numerical simulation on drop collision employs adaptive resolution, which uses nonuniform particle distribution instead of uniform particle distribution. The adaptive resolution can reduce unnecessary calculations and achieve a balance between calculation accuracy and efficiency.

The adaptive resolution used in this work was originally proposed by Yang and Kong [32]. The basic idea of adaptive particle distribution is as follows. Based on the distance between each particle and the interface, a reference spacing is defined, and the reference mass of the particle is determined accordingly. Then the ratio of the actual mass of this particle to its reference mass is calculated. If this ratio is larger than the critical value for particle splitting, the particle will be split

into two particles. On the contrary, if the mass ratio is less than the critical value for particle merging, the particle will be merged with a neighboring particle. As a consequence, an adaptive particle distribution is obtained.

To implement the adaptive resolution, a reference particle spacing is introduced, which varies with the distance between the selected particle and the interface of different phases. For particles that are further away from the interface, the reference particle spacing is larger and vice versa. Now introduce the concept of ‘‘particle band,’’ as shown in Fig. 2. The thick, black dashed line on the left side of the picture represents the interface. In the same particle band, the particles share the same value of reference spacing.

The width of the particle band is  $K\Delta S$ , where  $\Delta S$  is the reference particle spacing, and  $K$  is employed as a parameter controlling the width. The reference particle spacing of adjacent particle bands is defined as

$$\Delta S_{k+1} = C_r \Delta S_k, \quad (19)$$

where  $k$  denotes different particle bands.  $C_r$ , named the adaptive number, is defined as the ratio of the reference particle spacing between two adjacent particle bands. This parameter is introduced to control the degree of local refinement of particles. When  $C_r = 1$ , the particle bands are distributed with equal width and the reference particle spacing is uniform,

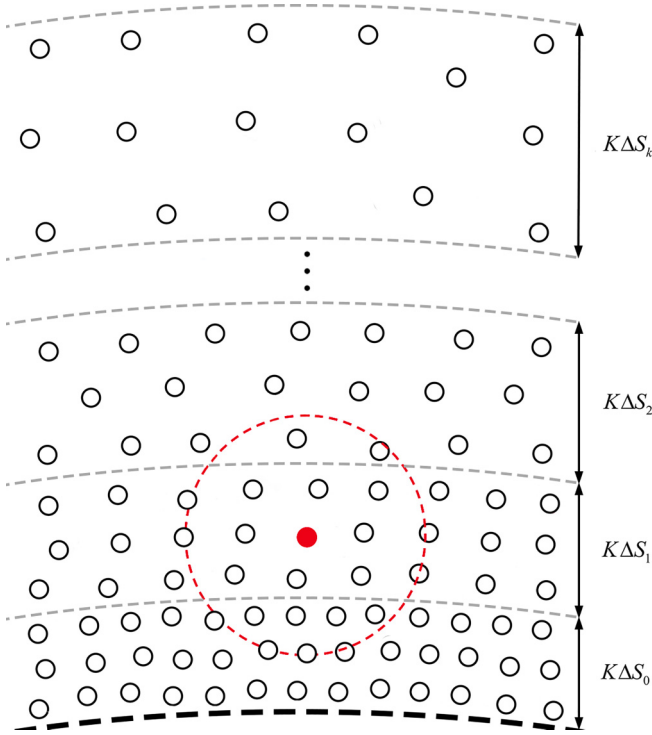


FIG. 2. Schematic diagram of particle band.

which does not lead to an adaptive resolution. When  $C_r > 1$ , the particle spacing becomes bigger with the increase of distance from the interface, and this trend accelerates with the enlargement of  $C_r$ . This means that the resolution of particles in the computational domain changes adaptively.

As shown in Fig. 2, the distance between the particles and the interface is determined by the particle band. The particle bands are found as follows: (a) Find the particles at the interface, (b) find the first particle band based on the distance between the particles and the interface particles, (c) find the next particle band based on the distance between the rest of the particles and the particles of the previous particle band, and (d) continue to find all the particle bands until there are no particles left outside the particle bands.

The adaptive distribution of particles is controlled by reference mass. In a two-dimensional simulation, the reference mass is defined as

$$m_r = \rho_r (\Delta S)^2. \quad (20)$$

Obviously, for particles of the same substance, the reference mass is related to the reference particle spacing. For a particle, if the ratio of its real mass to its reference mass is greater than the set value for particle splitting, we have

$$\frac{m}{m_r} > \gamma_s. \quad (21)$$

The particle will split into two smaller particles, the positions of which are calculated as follows:

$$\mathbf{r}_{i1,i2} = \mathbf{r}_i \pm \frac{\lambda}{2} \Delta s \mathbf{e}. \quad (22)$$

Here the subscripts  $i1$  and  $i2$  denote the two particles after the splitting of particle  $i$ ,  $\lambda = 0.6$ , and  $\mathbf{e}$  denotes the unit

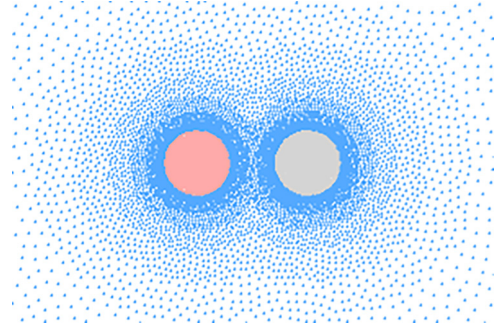


FIG. 3. Typical particle distribution of SPH method with adaptive spatial resolution.

vector perpendicular to the line connecting particles  $i$  and its nearest neighbor particle.

If the ratio is less than the set value for merging, we have

$$\frac{m}{m_r} < \gamma_m. \quad (23)$$

The particle will merge with its nearest neighbor particle. The position of the new particle is the center of the mass of the two particles before merging, which can be calculated as follows:

$$\mathbf{r}_k = \frac{m_i \mathbf{r}_i + m_j \mathbf{r}_j}{m_i + m_j}. \quad (24)$$

Here the subscript  $k$  denotes the new particle after merging;  $i$  and  $j$  denote the two particles before merging.

### III. BINARY COLLISION OF EQUAL-SIZE DROPS

In this section, the SPH-ASR method is utilized to perform numerical simulation on the collision of two water drops of equal diameter ( $\Delta = 1$ ). The typical distribution of particles based on the above adaptive resolution method is shown in Fig. 3. The dense and uniformly distributed particles are employed to precisely track the evolution of drop morphology during collision, while the adaptive resolution is applied in the surrounding gas to save computing resources. It should be noted that the simulations performed in the present paper are in two spatial dimensions. The spatial scale is referenced by the drop diameter. The computational domain is set to a rectangle 30 times the drop diameter in length and 20 times in width. The initial particle spacing is set to 1/40 of the drop diameter. The time step is set to 0.05 ms.

#### A. Verification

In order to verify the reliability of the numerical method presented in this paper, the simulation results are compared with the binary collision experiments of water drops by Ashgriz and Poo [9]. Within the scope of the main focus of this paper, two typical collision modes exist: coalescence and separation collision. For these two types of collision, the numerical results based on the adaptive SPH method can be in good agreement with the experimental results. As shown in Figs. 4 and 5, the numerical simulation images show high similarity with the experimental photos. The collision process

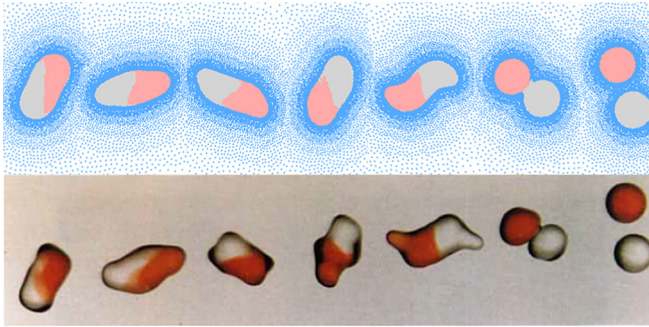


FIG. 4. Comparison of coalescence collision ( $We = 10, x = 0.5$ ) between SPH simulation (top) and experiment (bottom) [9].

and morphological characteristics of the drop are basically the same.

**B. Coalescence collision**

Figure 6 shows the process of head-on collision of two equal-size water drops at  $We = 3$ . It can be seen from the figure that the two water drops coalesce at first after contacting, forming a large drop. Subsequently, the coalesced drop contracts inward along the direction of the velocity vectors and pushes the liquid out from the center to form a flat disk or torus. At this time, the liquids on both sides meet on the central plane of impact and extend around, and then retreat in the directions perpendicular to the plane, driving the coalesced drop to stretch and deform outward. For the cases with relatively low Weber numbers, this reflexive motion cannot overcome the limit of surface tension of the coalesced drop, and the liquid mass will be pulled back and oscillate with amplitude attenuation. During this process, in addition to the large-scale oscillating deformation of the drop as a whole, small fluctuations propagating outward from the collision center were also observed on the surface. As a result, the two initial drops merge permanently to maintain a stable spherical shape. This type of collision is called “coalescence collision.”

Figure 7 shows the change in air pressure during the approach of liquid drops. As the two drops gradually move toward each other, the air pressure in the gap increases accordingly and reaches an extreme value at the minimum distance

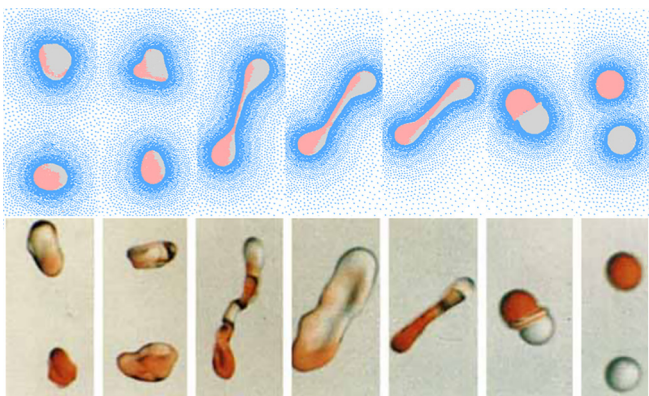


FIG. 5. Comparison of separation collision ( $We = 53, x = 0.38$ ) between SPH simulation (top) and experiment (bottom) [9].

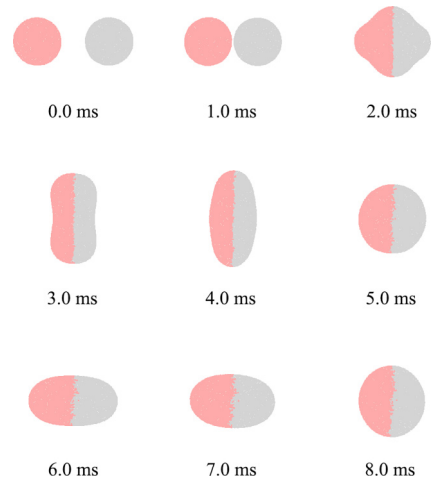


FIG. 6. Coalescence collision of equal-size drops at  $We = 3$  and  $x = 0$ .

between the drops. This phenomenon is consistent with the qualitative inference in the Introduction of this paper.

Figure 8 shows the evolution of pressure distribution in liquid drops during contact and deformation. As shown in Fig. 9(a), when two drops are in contact, the maximum pressure appears near the contact point due to extrusion at the impact area. From Figs. 8(b)–8(d), it can be seen that as the extrusion area extends on the symmetry plane of impact, the high-pressure area between the two drops also continues to expand, and the maximum pressure gradually shifts to the position with the maximum curvature at the upper and lower ends of the coalescing drop on the contact plane. When the two drops are completely coalesced, the maximum pressure inside is also transferred to the edge with large curvature. As shown in Figs. 8(e)–8(h), this area then expands to the indirect impact area on the left and right sides.

**C. Reflexive separation**

For the cases of head-on collision of two liquid drops, when the Weber number increases and exceeds a certain critical value, the coalesced drop will separate and generate two independent subdrops.

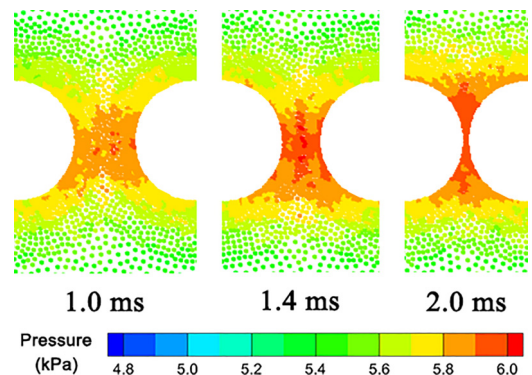


FIG. 7. Evolution of the nearby air pressure during the approach of liquid drops ( $We = 3, x = 0$ ).

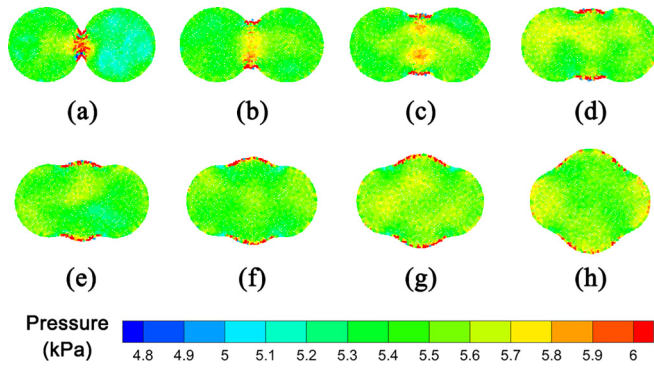


FIG. 8. Evolution of pressure inside the liquid drop(s) during impact ( $We = 3, x = 0$ ).

Reflexive separation is one of the subclasses of separation collision, which can also be said to be a special case of coalescence collision. In this type of collision, the motion of the inner part of the coalesced drop is similar to that in coalescence collision, but the intensity is increased. Due to the strengthening of the reflexive action, the mass of the coalesced drop is concentrated at both ends, forming a dumbbell-shaped liquid column, and finally pulling apart and separating into two subdrops. During the whole process, there is very little mass exchange on both sides of the collision system; that is, the composition of the subdrops is almost the same as that of the initial drops on the same side before the collision.

At the last stage before separation, because of the effect of surface tension and the movement of liquid, the radius of the connecting part of the liquid column gradually shrinks, forming an obvious necking band. The formation and fracture mechanisms of this necking band are one of the core issues in the study of separation collision. The pressure evolution in this process is shown in Fig. 9.

It can be seen from the figure that when the coalesced drop is about to separate, the pressure at the necking zone increases significantly, and the capillary potential energy of the system reaches a maximum, which is consistent with the “end-pinching” theory proposed by Stone *et al.* [40]. Then the necking band breaks instantaneously, and the pressure propagates rapidly to both sides in opposite directions (this is also proved by the instantaneous loss of pressure of the residual particles between the two subdrops). During this process, the capillary potential energy accumulated in the necking zone provides kinetic energy for the split subdrops to move away from each other, and causes significant fluctuations on the surface. This part of the energy is gradually dissipated with

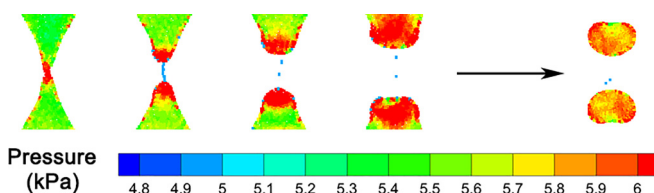


FIG. 9. Evolution of pressure at the moment of separation ( $We = 30, x = 0$ ).

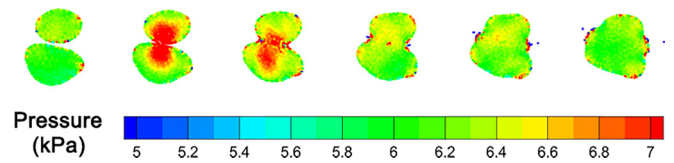


FIG. 10. Evolution of pressure during the recoalescence of satellite drops ( $We = 119, x = 0$ ).

the internal viscous flow of subdrops, and the oscillation is also attenuated.

As the Weber number continues to increase, the coalesced drop generated by impact elongates significantly, forming a narrower and longer liquid column. When the Weber number reaches a certain critical value, a “satellite” drop with mixed mass is formed between the previous two subdrops. The satellite drop has no regular shape at the beginning of its generation, and only becomes stably circular after a long period of oscillation. If the Weber number increases further, the volume of the satellite drop will continue to increase and gradually exceed the primary drops on both sides, presenting more violent oscillations. When the intensity of the internal flow exceeds the limit that the surface tension can withstand, the satellite drop will continue to split from the sides to the center, generating multiple smaller subdrops. In this case, the satellite drops are still arranged roughly along a straight line, while the amount increases with the increase of the Weber number.

At higher Weber numbers, the recoalescence of closely adjacent satellite drops disconnected from the coalesced liquid column is observed. Compared with the primary drops and other satellites, the satellite drops near the middle have little remaining kinetic energy when they break away from the liquid column, and the relative motion between them is very weak. At this point, the adjacent satellite drops may make contact again and recombine. Due to the extremely low speed upon contact, coalescence occurs slowly under the control of intermolecular forces [11]. When the smallest gap between the drop interfaces reaches the range of molecular interactions (usually of the order of  $102 \text{ \AA}$ ) [41], the gas film in the middle is discharged, and the drops come into contact, forming a long coalesced drop. Subsequently, the drop is pulled into a sphere by surface tension, essentially without oscillations. The pressure distribution inside the drops during this process is shown in Fig. 10. It can be seen that the pressure gradient inside the drops is significantly smaller than that at the moment of previously mentioned impact, and the pressure distribution presents a gradual characteristic, which quickly returns to the normal level.

To be distinguished from the aforementioned coalescence collision (designated “hard collision”), this situation is also referred to as “soft collision” [42], or “coalescence after minor deformation.” In hard collision, the gas film between the drop interfaces is squeezed out forcibly, and the facing region of both drops is significantly deformed. Coalescence occurs when the impact inertia is sufficient to overcome both the viscous loss caused by drop deformation and the gas resistance in the gap, so in this case, the coalescence behavior is mainly induced by the initial kinetic energy of the drops.

However, in soft collision, the drops' approach speed is low, the gas film has enough time to slowly release, and the drops' shape does not change dramatically. According to the analysis of previous experimental works about soft collision [11], the contact and the following combination of drops are mainly related to intermolecular effects.

When the liquid drops' approach rate is between the above two states, there is an intermediate state whose initial kinetic energy is sufficient to rapidly squeeze the gas film, creating a large resistance and causing significant deformation of the drops, but it is unable to further compress the gas film to achieve contact. In this process, the kinetic energy is first fully converted into capillary potential energy with a small amount of dissipation, and then converted back into kinetic energy, resulting in drop rebound. This collision mode has also been confirmed in some experimental works [11,42,43].

However, due to the relatively high surface tension and low viscosity, water drops are usually less deformed with less viscous dissipation than other materials such as hydrocarbons, and thus are more prone to coalesce, especially in collisions with lower Weber numbers. Therefore, as mentioned in the Introduction, bouncing collision is unlikely to occur in the binary collision of water drops at 1 atm pressure without artificially controlling gas density [11]. Another result that follows is that although the two types of coalescence collision based on soft and hard collision have different physical mechanisms, it is difficult to determine the boundaries of their influencing factors through intuitive collision phenomena. However, the soft collision can be easily identified in the recoalescence phenomenon of reflexively separated satellite drops, because there is theoretically no strong opposite motion between sub-drops, which means that the gas film in the gap cannot be compressed sharply.

It is worth mentioning that such drop coalescence is usually difficult to simulate with traditional numerical methods. For those grid based methods coupled with interface capturing technology, the identification of merging surfaces usually meets difficulty at lower Weber numbers. As a possible consequence, the coalescence after minor deformation is erroneously represented as bouncing collision; that is, the impact inertia cannot overcome the gas film resistance [44]. For the SPH method, since all the objects are described by different sets of material particles possessing physical properties, the interacting regions are formed naturally, so the destruction and regeneration of interfaces can be better reflected.

#### D. Stretching separation

Taking the off-center collision of water drops as an example, consider the cases where the impact parameter  $x \neq 0$ . Due to the eccentricity between the two drops in the direction perpendicular to the relative velocity, only a portion of the mass interacts upon impact, decelerating and spreading along the tangent of the contact, while the rest is dominated by inertia and has a tendency to stretch the coalesced drop along the direction of initial velocity. Thus, the reflexive motion of the coincident part is opposed to the facing motion of the noncoincident part, and the entire collision process can be regarded as the superposition of the two actions. In this situation, the

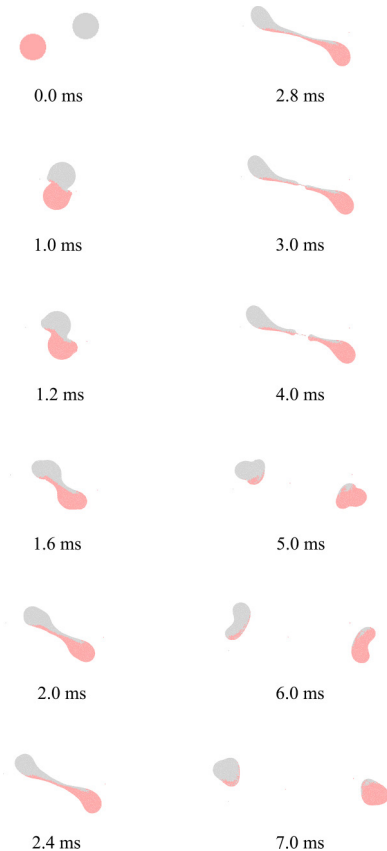


FIG. 11. Stretching separation collision of equal-size drops at  $We = 53$  and  $x = 0.8$ .

mass transfer between the two drops becomes more obvious, with the flow inside the drops being more complicated.

It is conceivable that there is a critical point of “equal strength” for the above two competing effects. In this range, the residual kinetic energy is no greater than the surface energy of the coalesced drop. As the impact parameter continues to increase, the effect of the opposite stretching motion will gradually surpass that of the reflexive separating motion, and thus it dominates the outcomes of collision. Separation occurs when the residual kinetic energy exceeds the surface energy, which is referred to as stretching separation. The typical process of stretching separation collision is shown in Fig. 11. It can be seen that the drop system has undergone significant stretching deformation during the process, accompanied by obvious mass migration inside. Finally, subdrops with mixed masses are generated. The main masses of the two initial drops exchange their positions after collision and move to each other's half area, respectively.

In stretching separation collision, the effective kinetic energy comes from the inertial motion of the nonoverlapping part and the tangential motion of the overlapping parts along the contact plane. It is commonly recognized that the effective kinetic energy overcomes the surface energy of the interacting region, which leads to the final separation. However, by further investigating the evolution of drop morphology and velocity distribution during the process, we found that the entire system has actually experienced quite complex varia-

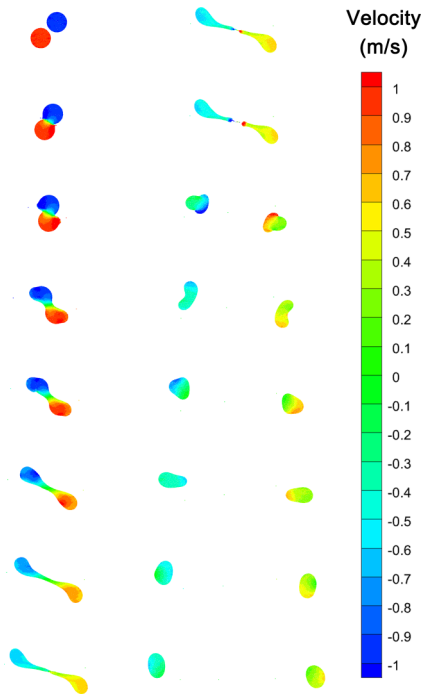


FIG. 12. Evolution of horizontal velocity distribution in stretching separation ( $We = 53$ ,  $x = 0.8$ ).

tions. Figure 12 shows the distribution and evolution of the horizontal velocity of the drops during the stretching and separation process.

The first column of Fig. 12 shows the process from the impact of the drops to the moment before separation. At the moment of contact, a region with zero velocity is formed between two opposing drops, which can be seen as the result of the counterbalance between the reflexive movement and the stretching movement of the drop system. Subsequently, the noncoincident parts of the system maintain the original state of motion under the action of inertia, pulling the coalesced drop to stretch and deform on both sides, while a necking band is formed in the middle. Meantime, the static area also continues to elongate under the action of stretching, with the affected area gradually expanding. Being dragged by the central part, both ends of the coalesced liquid column experience a continuous decrease in velocity, which means that the remaining kinetic energy of the noncoincident parts of the drop system is being transformed into the increment of capillary potential energy. It is worth mentioning that not only the mass connected to the necking band is dragged, but the liquid at both ends of the liquid column is also decelerated under the action of local surface tension.

It is noted that due to the nonaxisymmetric nature of the drop system, the separating motion at both ends of the liquid column is not uniformly restrained. The liquid on the extension line of the necking zone has a greater decline in kinetic energy, while the other parts still maintain a relatively high velocity. These high-speed liquids pull the coalesced liquid column to further stretch and gradually occupy the positions at both ends of the liquid column.

In the collision experiments performed on tetrad cane droplets by Qian and Law [11], the overall rotation of the

coalesced drop was also observed. From the numerical simulation in the present paper, we can determine with confidence that this rotational motion occurs after the first stretching of the coalesced drop. Before extending to the maximum length, both ends of the coalesced column maintain translational motion, and the subsequent angular velocity is imparted by the tension of the necking band. As can be seen from Fig. 12, this asymmetrical tension acts more on the inner side of the coalesced system, thus shortening the liquid column in the length direction on the one hand, and producing a rotational motion on the other hand.

The process after separation is shown in the second column of Fig. 12. When the necking band breaks, the tips of the two subdrops rapidly rebound and collapse into tail ends with high kinetic energy. Meanwhile, with the air resistance ignored, the local speed at the far ends of the subdrops continues to decrease since the overall total momentum remains basically unchanged. When the tips are fully contracted, the velocity in these areas has almost dropped to 0. Then, the tail ends with relatively higher speed push the subdrops to continue moving oppositely along their initial directions. After that, although the drop system maintains approximately translational motion, and the internal liquid composition still has a relatively stable distribution, its deformation and oscillation are not completely symmetrical. It can be observed that on top of the reciprocating oscillations of the overall drop shape in mutually orthogonal directions, a surface wave propagating in the counterclockwise direction is superimposed, and the curvature increases as it passes. This rotational motion is also caused by the nonuniformity of the system mentioned above. Compared with the overall rotation of the coalesced column mentioned above, here the motion occurs mainly on the surface of subdrops. Under the effects of large-scale deformation and oscillation, the speed of the drops decreases sharply.

Looking back at the entire stretching separation process, we can clearly see the path of energy conversion. After impact, the remaining kinetic energy of the initial drops is first transformed into the capillary potential energy of the coalesced system. With the fracture and contraction of the necking band, the capillary potential energy returns kinetic energy to the separated drops. In the end, the kinetic energy of drops is continuously dissipated along with the oscillation, and the system tends to be stable.

### E. Phase diagram

Figure 13(a) shows the regimes of drop collision obtained from numerical simulations compared with experiments from the literature. The range of Weber numbers in the numerical simulation is  $3 \leq We \leq 120$ , and the range of impact parameter is  $0 \leq x \leq 0.8$ . The curves are obtained from the analytical models provided by Ashgriz and Poo [9], which are in good agreement with the experimental results and are widely adopted as a reference. The experimental results for equal-size water drop collisions under the same conditions are shown in Figs. 13(b) and 13(c). Compared with the experimental results, the present numerical simulations have some difficulty in identifying the coalescence collision with the impact parameter lying between the two collision-mode boundaries at Weber numbers higher than 20. This is

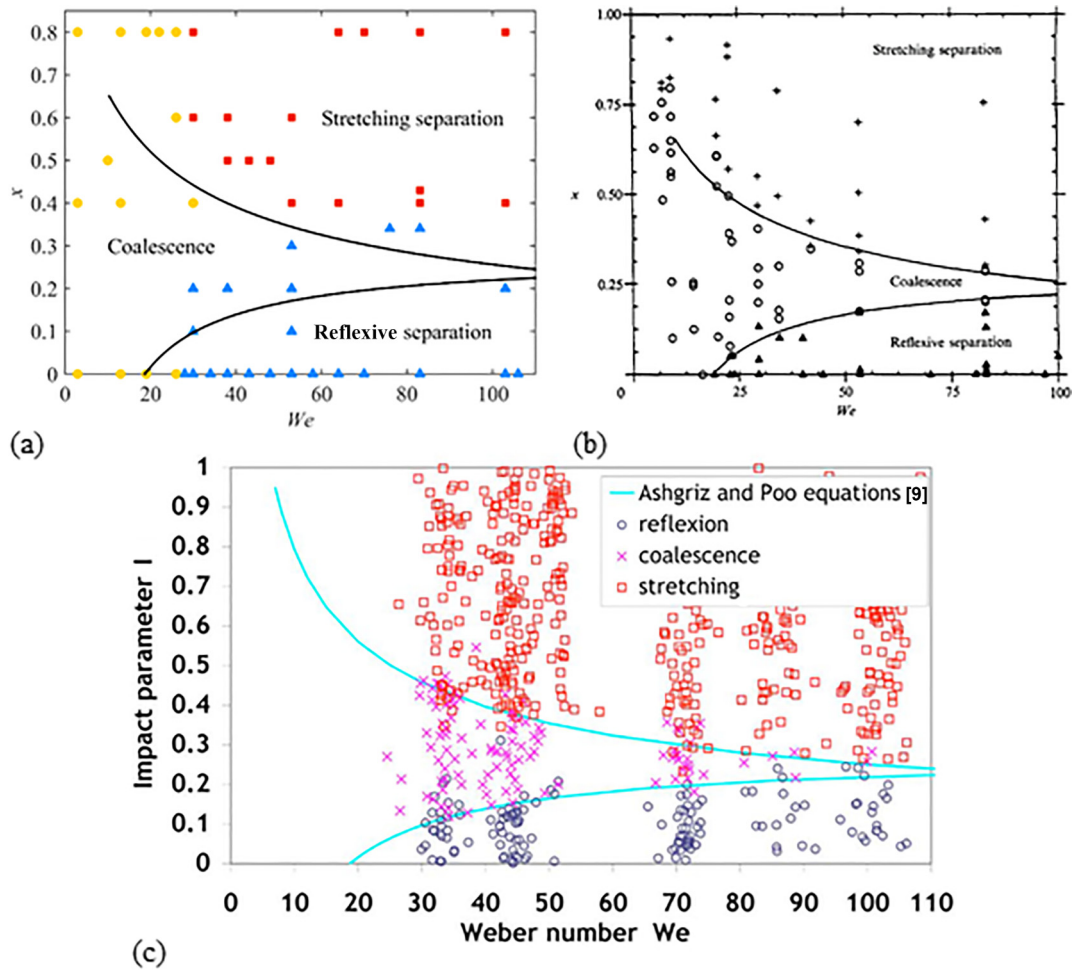


FIG. 13. Regime diagram of equal-size drop collision: (a) obtained from numerical simulation with the present SPH method, (b) reproduced from experiments by Ashgriz and Poo [9], and (c) reproduced from experiments by Rabe *et al.* [45].

mainly due to the higher ratio of the internal flow kinetic energy to the surface energy of the nominal spherical drop in two-dimensional simulations, which makes it easier for the coalesced drop to separate.

#### IV. BINARY COLLISION OF UNEQUAL-SIZE DROPS

Although the binary collision of equal-size drops plays a rather basic part in research, it is very rare see it in reality. In order to obtain a deeper understanding of the physics in drop collision problems, it is quite necessary to investigate the collision of unequal-size drops. In such problems, our primary concern is undoubtedly the variation law of the collision phenomenon with the drop diameter ratio, which is the starting point of this section.

Compared with equal-size drops, one of the significant features of unequal-size drop collisions is that there are parts in the system that do not directly participate in the collision. These liquids have a tendency to maintain the original state of motion and thus have a significant pulling effect on the mass of other parts. In addition, the pressure asymmetry on the two sides of the drop system due to different curvatures will lead

to additional flow along the axis, increasing the complexity of the phenomenon.

##### A. Coalescence collision

The head-on collision of drops with a diameter ratio of 0.5 at  $We = 30$  is shown in Fig. 14. A translation of the whole system is observed, which shares the same direction with the initial velocity of the larger drop. Looking back at Fig. 13, it can be seen that under the current Weber number of 30, the equal-size drops have undergone reflexive separation, while the unequal-size drops still remain coalesced. In this situation, the kinetic energy injected by the smaller drop into the larger one is not enough to break the limit of overall surface tension, which is consistent with our intuitive impression. It can be concluded from this phenomenon that two drops of different sizes are more difficult to separate after collision, so a higher Weber number is usually required for the occurrence of separation collision.

It is also observed that the coalesced drop generated by unequal-size drops has relatively slower oscillation. This is mainly caused by the additional inertial force introduced by the larger drop, since the oscillation period of the coalesced

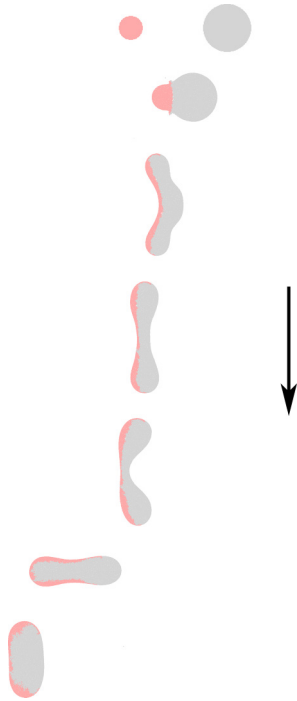


FIG. 14. Coalescence collision of unequal-size drops with  $\Delta = 0.5$  ( $We = 30, x = 0$ ).

drop is negatively related to the inertial force. In the initial stage of collision, the velocity of the smaller drop decreases more significantly, as shown in Fig. 15. As the drop diameter ratio increases, the stagnation point of liquid flow shifts to the side of the smaller drop. For the cases with larger differences in drop size, as shown in Figs. 15(b) and 15(c), the stagnation point is almost completely located in the small drop.

For the collision of unequal-size drops, the coalesced body formed after contact no longer expands into a symmetrical disk shape on the impact plane, but a “bowl” shape recessed to one side. This phenomenon starts with the liquid splash at the vicinity of the contact point, as shown in Fig. 16. It can be seen in the figure that the splashed liquid comes from both of the two drops, which indicates two related actions that are almost equally important. On the one hand, the directly impacted part in the larger drop changes its original trajectory and deflects to both sides of the stagnation point. On the other hand, the edge

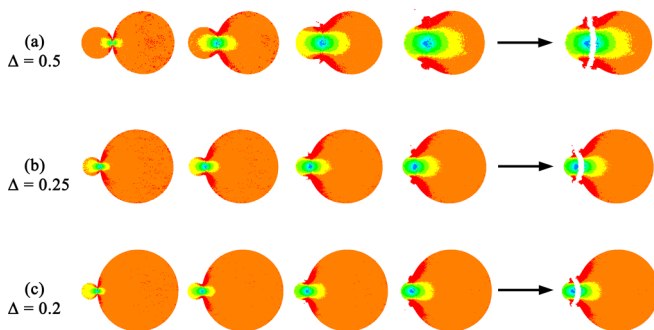


FIG. 15. Evolution of velocity distribution in drop systems with different diameter ratios ( $We = 30, x = 0$ ).

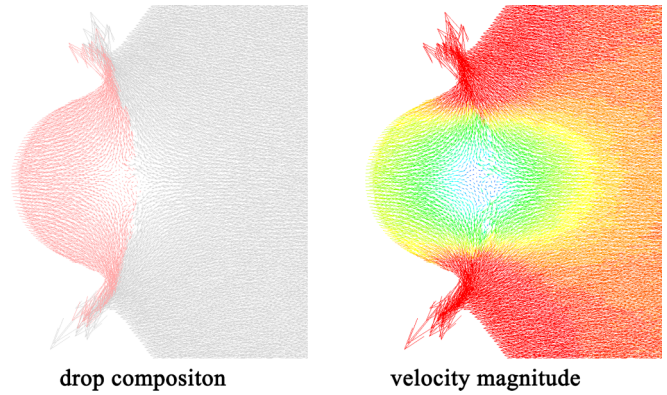


FIG. 16. Distribution of velocity vectors at the impact area ( $We = 30, \Delta = 0.25$ ).

part of the smaller drop obtains a reverse movement due to the impact of the opposite part of the larger drop. The above two parts converge and extend along the interface of two drops to the outside of the overall envelope, forming a splashing phenomenon.

Subsequently, the liquid in the smaller drop merges into the coalesced drop and expands to both sides, while the unimpacted part of the larger drop tends to maintain its original state of motion. The splashing phenomenon is thus intensified, and gradually develops from local flow to the bending of the whole coalesced drop, as shown in Fig. 17.

The above bending phenomenon results in a special oscillation mode. In these circumstances, the coalesced drop not only oscillates alternately along two mutually orthogonal directions, but also shows mass flow back and forth between both ends of the drop along the axis. This process is shown in Fig. 18. The energy comes from the kinetic energy of the nonimpacting part of the larger drop, which is gradually dissipated with the round trips of the liquid.

**B. Separation collision**

In the separation collision of unequal-size drops, many phenomena, such as the formation and evolution of satellite drops, are very similar to those in the collision of equal-size drops. However, for the cases where only two subdrops are generated, we can often observe the unique phenomenon where the drop diameter ratio changes after collision. The redistribution of mass usually causes significant changes in the morphology of drop systems, especially in spray fields containing a large number of drops.

Experiments have proved that the reflexive separation collision of unequal-size drops usually leads to the uniformity of drop mass in the system; that is, the volume difference

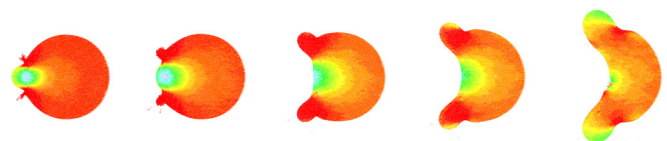


FIG. 17. Coalescence process of unequal-size drops ( $We = 30, \Delta = 0.25$ ).



FIG. 18. Shape development of coalesced drop ( $We = 30$ ,  $\Delta = 0.5$ ).

between two drops decreases after collision. However, in stretching separation collision, results of both increased or decreased mass difference may occur [9]. That means the physical mechanisms controlling the two collision modes should not be exactly the same.

The separation collision of unequal-size drops can often reflect the antagonism of two opposing effects. One is the same for reflexive and stretching separation collisions, which is called “drop drainage.” As shown in Fig. 19, this is a phenomenon in quasistatic flows. When two drops of different sizes come into contact and form a connected area, there is an additional pressure difference at both ends of the coalesced drop due to different surface curvatures, which leads to a tendency of liquid to flow from the smaller drop to the larger one. From the energy point of view, this flow will reduce the capillary potential energy of the system, thereby gradually stabilizing.

In reflexive separation, the other antagonistic effect is the axial mass movement mentioned in Sec. IV A. Since two drops collide head on (or nearly head on) at a relatively high speed in this situation, the smaller drop only maintains its shape and curvature for a very short time, and soon merges into the coalesced body. Therefore, the quasistatic drop drainage effect does not have enough time to fully take effect. In contrast, the phenomenon of axial mass transfer is a dynamic effect and thus plays a more critical role. After the coalesced drop is formed, this action transports an amount of liquid to one end of the original smaller drop, resulting in an increase in the volume of the smaller subdrop after reflexive separation, that is, “carrying away” some mass from the larger drop. As a consequence, the drop system is homogenized to a certain extent. The above discussion is consistent with the outcomes observed in previous experiments.

For stretching separation, the other dominating effect is different, called “drop stretching.” This effect, which refers to the mutual cutting action of drops when eccentric collision occurs, also exists in collisions of equal-size drops, but for two drops of different sizes, the cutting effect of each drop is not equal due to the geometric asymmetry of the collision system. A comparison is shown in Fig. 20. As can be seen from Fig. 20(b), the mass lost by the smaller drop is significantly less than the mass it gains from the larger drop. In other words,

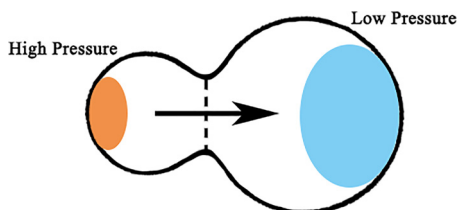


FIG. 19. Schematic diagram of drop drainage effect.

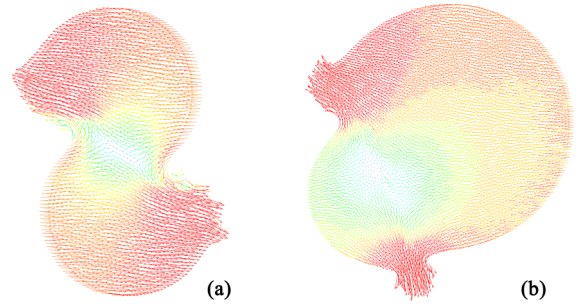


FIG. 20. Comparison between the cutting effects of equal-size and unequal-size drops (in velocity vectors).

more liquid in the larger drop is “cut” away and becomes part of the smaller subdrop.

In stretching separation, only some parts of the two drops come into contact, so their geometrical shapes and edge curvatures can be maintained for a relatively long time. In this situation, both the effects of “drop drainage” and drop stretching are very significant, and thus their relative strength will determine the diameter ratio of the generated subdrops. The drop drainage effect helps to expand the size difference of the subdrops, while the drop stretching effect works oppositely. For collision systems with their initial drop diameter ratio determined, the strength of the two effects is related to the impact parameter and Weber number.

With the increase of impact parameter, the geometric centers of two drops become farther apart. As a result, the smaller drop will cut off less mass of the larger drop, and the drop stretching effect will be weakened. As shown in Fig. 21, the size of the smaller subdrop is negatively correlated with the impact parameter. In addition, as the impact parameter increases, the mixing degree of the two drops is also reduced, indicating that the cutting effect is weakening.

With the increase of Weber number, the drop system has a higher relative speed and a shorter contact time. As a result, the mass transfer caused by the pressure difference between both ends cannot be fully carried out, and thus the drop drainage effect is weakened.

It can be deduced that the sizes of the subdrops should be more similar, which has been proved by previous experiments [9]. However, we found that this pattern is not absolute. In fact, due to the intense flow under higher Weber numbers, the coalesced body deforms rapidly. Some liquid may break through the limit of the surface tension locally and fracture before the cutting action is completed, so a series of subdrops with smaller volume and higher degree of fragmentation is often observed, as shown in Fig. 22. This phenomenon usually occurs when the size difference of the initial drops is not

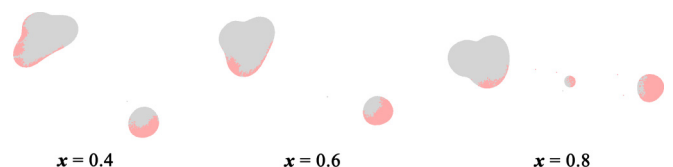


FIG. 21. Comparison of the subdrop sizes of stretching separation under different impact parameters ( $We = 43$ ,  $\Delta = 0.5$ ).

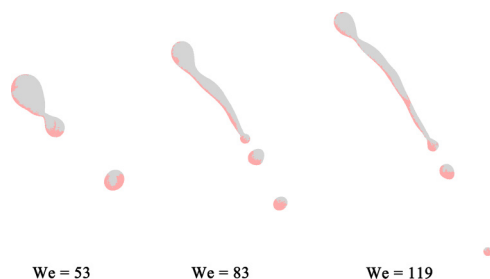


FIG. 22. Comparison of the subdrop sizes of stretching separation under different Weber numbers ( $\Delta = 0.5$ ,  $x = 0.4$ ).

too small and the impact parameter is not too large. In this situation, most of the mass of the smaller drop is involved in the impact, and the generated subdrops can also be regarded as a result of the resplit of the coalesced drop.

## V. CONCLUSIONS

In this paper, the binary collision problem of water drops in air is numerically simulated by the SPH-ASR method. The simulation outcomes are compared with experimental results. The agreement between the numerical and experimental results indicates that the SPH-ASR method presented in this paper is suitable for the simulation of the drop collision problem.

Using the SPH-ASR method, a number of numerical simulations were performed to study the collision of binary drops. The collision of two equal-size drops was studied with the focus on the specific phenomena, evolution patterns, and physical principles. It is demonstrated that there are three basic collision modes in the binary collision of equal-size drops within the range of Weber number  $3 \leq We \leq 120$  and impact parameter  $0 \leq x \leq 0.8$ : coalescence, reflexive separation, and stretching separation. For coalescence collision, the variation of air pressure and liquid pressure in the system was intensively investigated. For reflexive separation, the necking process, being a symbol of separation, was depicted in full steps, which supports the end-pinching theory on the

formation and fracture process of the necking band proposed in the literature [40]. With the evolution of pressure distribution, the propagation of the surface wave was shown clearly. At higher Weber numbers, the recoalescence of satellite drops was investigated as a good supplement to the regimes of coalescence collision. It is proved that the SPH-ASR method has obvious advantages in simulating the evolution of interfaces. For stretching separation, the morphological and kinematic processes of the drops were described in detail, which indicated the path of energy conversion in the collision system. By analyzing the velocity distribution and evolution of the collision system, the rotational motion of the subdrops after separation is discovered, and the differences in phenomenon and principle between this rotation and the overall rotation observed in Qian and Law's experiments [11] are expounded.

The collision of two drops with different sizes is also studied. The effects of the three dimensionless numbers, namely, the drop diameter ratio, Weber number, and impact parameter, on collision outcomes are studied. In particular, the physical mechanisms of some special phenomena are explained, especially the oscillation pattern of coalescence collision and the mass transfer in separation collision. It is shown by numerical simulation that there are two main roots for those special phenomena: (a) the geometric asymmetry of the drop system, that is, the quasistatic flow caused by the irregularity in the shape of the system, which is typically manifested by the additional pressure difference caused by different surface curvatures; and (b) the motion asymmetry of the drop system, that is, the motion tendency caused by the unequal motion properties of different parts of the system, which is typically manifested by the spillover kinetic energy of the nonimpact part of the larger drop. In addition, there are some influencing factors that reflect the above two points at the same time, such as the drop stretching effect. Sometimes, both of the above two points work at the same time, as seen in the drop stretching effect.

## ACKNOWLEDGMENTS

This work was supported by the National Natural Science Foundation of China (Grant No. 12172049).

- 
- [1] S. Suo, M. Jia, H. Liu, and T. Wang, *Int. J. Multiphase Flow* **137**, 103581 (2021).
  - [2] S. L. Post and J. Abraham, *Int. J. Multiphase Flow* **28**, 997 (2002).
  - [3] J. M. MacInnes and F. V. Bracco, *Numer. Approac. Combust. Model.* **615** (1991).
  - [4] S. Jafarmadar and P. Nematy, *Energy* **93**, 2280 (2015).
  - [5] B. J. de Gans and U. S. Schubert, *Macromol. Rapid Commun.* **24**, 659 (2003).
  - [6] S. Fathi, P. Dickens, and F. Fouchal, *J. Mater. Process. Technol.* **210**, 550 (2010).
  - [7] W. Qiang and G. Liang, *Chin. J. Aeronaut.* **30**, 1391 (2017).
  - [8] P. R. Brazier-Smith, S. G. Jennings, and J. Latham, *Proc. R. Soc. London, Ser. A* **326**, 393 (1972).
  - [9] N. Ashgriz and J. Y. Poo, *J. Fluid Mech.* **221**, 183 (1990).
  - [10] Y. J. Jiang, A. Umemura, and C. K. Law, *J. Fluid Mech.* **234**, 171 (1992).
  - [11] J. Qian and C. K. Law, *J. Fluid Mech.* **331**, 59 (1997).
  - [12] C. Planchette, E. Lorenceau, and G. Brenn, *Fluid Dynam. Mater. Proc.* **7**, 279 (2011).
  - [13] T. Marić, D. B. Kothe, and D. Bothe, *J. Comput. Phys.* **420**, 109695 (2020).
  - [14] X. Chen and V. Yang, *Phys. Fluids* **32**, 062103 (2020).
  - [15] B. Boyd and Y. Ling, *Comput. Fluids* **254**, 105807 (2023).
  - [16] F. Gibou, R. Fedkiw, and S. Osher, *J. Comput. Phys.* **353**, 82 (2018).
  - [17] M. Chai, K. Luo, C. Shao, S. Chen, and J. Fan, *Chin. J. Chem. Eng.* **25**, 1 (2017).
  - [18] L. Scarbolo, F. Bianco, and A. Soldati, *Phys. Fluids* **27**, 073302 (2015).

- [19] A. Kajzer and J. Pozorski, *Comput. Math. Appl.* **106**, 74 (2022).
- [20] C. Shao, S. Yuan, and K. Luo, *J. Comput. Phys.* **487**, 112158 (2023).
- [21] M. Yousefzadeh, Y. Yao, and I. Battiato, *J. Comput. Phys.* **478**, 111958 (2023).
- [22] L. B. Lucy, *Astron. J.* **82**, 1013 (1977).
- [23] R. A. Gingold and J. J. Monaghan, *Mon. Not. R. Astron. Soc.* **181**, 375 (1977).
- [24] J. J. Monaghan, *J. Comput. Phys.* **110**, 399 (1994).
- [25] X. Y. Hu and N. A. Adams, *J. Comput. Phys.* **213**, 844 (2006).
- [26] C. Antoci, M. Gallati, and S. Sibilla, *Comput. Struct.* **85**, 879 (2007).
- [27] H. H. Bui, R. Fukagawa, K. Sako, and S. Ohno, *Int. J. Numer. Anal. Methods Geomech.* **32**, 1537 (2008).
- [28] W. Benz and E. Asphaug, *Comput. Phys. Commun.* **87**, 253 (1995).
- [29] R. Vacondio, C. Altomare, M. De Leffe, X. Hu, D. Le Touzé, S. Lind, J.-C. Marongiu, S. Marrone, B. D. Rogers, and A. Souto-Iglesias, *Comput. Part. Mech.* **8**, 575 (2021).
- [30] S. Watanabe and T. Aoki, *Comput. Phys. Commun.* **264**, 107871 (2021).
- [31] C.-M. Wu, Y.-S. Zhou, and C.-A. Lin, *Comput. Fluids* **210**, 104647 (2020).
- [32] X. Yang and S.-C. Kong, *Comput. Phys. Commun.* **239**, 112 (2019).
- [33] X. Yang, S.-C. Kong, M. Liu, and Q. Liu, *J. Comput. Phys.* **443**, 110539 (2021).
- [34] X. Yang, S.-C. Kong, and Q. Liu, *Phys. Rev. E* **104**, 055308 (2021).
- [35] T. Breinlinger, P. Polfer, A. Hashibon, and T. Kraft, *J. Comput. Phys.* **243**, 14 (2013).
- [36] X. Yang and M. Liu, *Acta Phys. Sin.* **61**, 224701 (2012).
- [37] X. Yang, M. Liu, and S. Peng, *Comput. Fluids* **92**, 199 (2014).
- [38] L. Hernquist and N. Katz, *Astrophys. J. Suppl. Ser.* **70**, 419 (1989).
- [39] J. J. Monaghan, *Annu Rev Fluid Mech* **44**, 323 (2012).
- [40] H. A. Stone, B. J. Bentley, and L. G. Leal, *J. Fluid Mech.* **173**, 131 (1986).
- [41] G. D. M. MacKay and S. G. Mason, *Can. J. Chem. Eng.* **41**, 203 (1963).
- [42] K.-L. Pan, C. K. Law, and B. Zhou, *J. Appl. Phys.* **103**, 064901 (2008).
- [43] M. Orme, *Prog. Energy Combust. Sci.* **23**, 65 (1997).
- [44] Y. Pan and K. Suga, *Phys. Fluids* **17**, 082105 (2005).
- [45] C. Rabe, J. Malet, and F. Feuillebois, *Phys. Fluids* **22**, 047101 (2010).